NDT&E International 163 (2026) 103790

Contents lists available at ScienceDirect

NDT and E International

journal homepage: www.elsevier.com/locate/ndteint

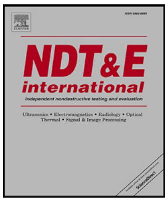

Research Paper

Super-resolution ultrasonic Lamb wave imaging via dispersion-embedded deconvolution

Tingjian Li [b,c], Shanwu Li [a], Shengbo Shan [d], Li Cheng [b], Yongchao Yang [a,*]

[a] School of Civil Engineering, Harbin Institute of Technology, Harbin, 150090, China
[b] Department of Mechanical Engineering, The Hong Kong Polytechnic University, Hong Kong, China
[c] College of Engineering, Eastern Institute of Technology, Ningbo, 315200, China
[d] Laboratory of Science and Technology on Integrated Logistics Support, College of Intelligent Science and Technology, National University of Defense Technology, Changsha, 410073, China

ARTICLE INFO

Keywords:
Diffraction limit
Total focusing method
Deconvolution algorithms
Super-resolution imaging

ABSTRACT

Enhancing the spatial resolution of ultrasonic Lamb wave imaging, fundamentally bounded by the diffraction limit, remains an important challenge in nondestructive testing (NDT). Seeking to exceed such a resolution limit, i.e., *super*-resolution (SR), is a difficult ill-posed inverse problem. While it may be directly and effectively interpreted as a deconvolution process, Lamb wave SR imaging is uniquely complicated by the significant dispersion nature of Lamb waves, which renders the system point spread function (PSF) inherently frequency-, mode-, and space-dependent. In this work, we develop a dispersion-informed deconvolution framework for SR imaging by explicitly embedding the Lamb-wave dispersion physics into the PSF modeling. Specifically, physically consistent PSF is incorporated into the total focusing forward model, enabling inversion of dispersion-induced blurring and recovery of structural details that are irreversibly lost in conventional array images. Validations are performed through finite element simulations and laboratory experiments on aluminum plates. It is observed that the proposed framework achieves reliable super-resolution separation of closely-spaced defects beyond the classical diffraction limit while maintaining robustness under low signal-to-noise ratio (SNR) conditions. In particular, a comprehensive parametric study is conducted to elucidate the key factors governing its super-resolution capability. It is revealed that a larger effective aperture enhances spatial focusing and resolution, while denser sensor spacing improves PSF fidelity and inversion stability under dispersive propagation. Discussions including challenges identified in this study are presented.

1. Introduction

Ultrasonic array imaging has become an indispensable tool for detecting and localizing hidden damage in plate-like structures, owing to its capabilities for rapid scanning, wide-area coverage, and real-time visualization [1–3]. When combined with guided Lamb waves, array-based inspection further benefits from long propagation distances and multi-modal interactions with structural defects. Using controlled time delays across the elements of the array, Lamb-wave arrays enable dynamic beam steering and synthetic focusing under waveguiding conditions, significantly enhancing defect detectability in applications of structural health monitoring (SHM) and nondestructive testing (NDT) [4–8].

Despite these advantages, the spatial resolution of ultrasonic array imaging is fundamentally constrained by wave diffraction. For array-based methods, the minimum resolvable distance between two scatterers is ultimately bounded by the wavelength of the propagating mode, as formalized by the Rayleigh criterion [9,10]. This limitation imposed by diffraction leads to blurred reconstructions when defects are closely spaced or subwavelength in size, which motivates extensive research into super-resolution imaging techniques that aim to surpass this classical boundary [11–14].

Among the various super-resolution strategies developed to overcome the diffraction limit, subspace-based methods such as time-reversal multiple signal classification (TR-MUSIC) have attracted considerable attention [15–17]. By exploiting the orthogonality between signal and noise subspaces of the time-reversed scattering matrix, TR-MUSIC can theoretically achieve localization beyond the diffraction limit [18–21]. However, its practical applicability in NDT is often limited by pronounced sensitivity to measurement noise and the requirement for multiple-input multiple-output (MIMO) configurations, which substantially increase system complexity and reduce robustness

---

* Corresponding author.
E-mail address: yangyongchao@hit.edu.cn (Y. Yang).

https://doi.org/10.1016/j.ndteint.2026.103790
Received 3 March 2026; Received in revised form 17 May 2026; Accepted 29 May 2026

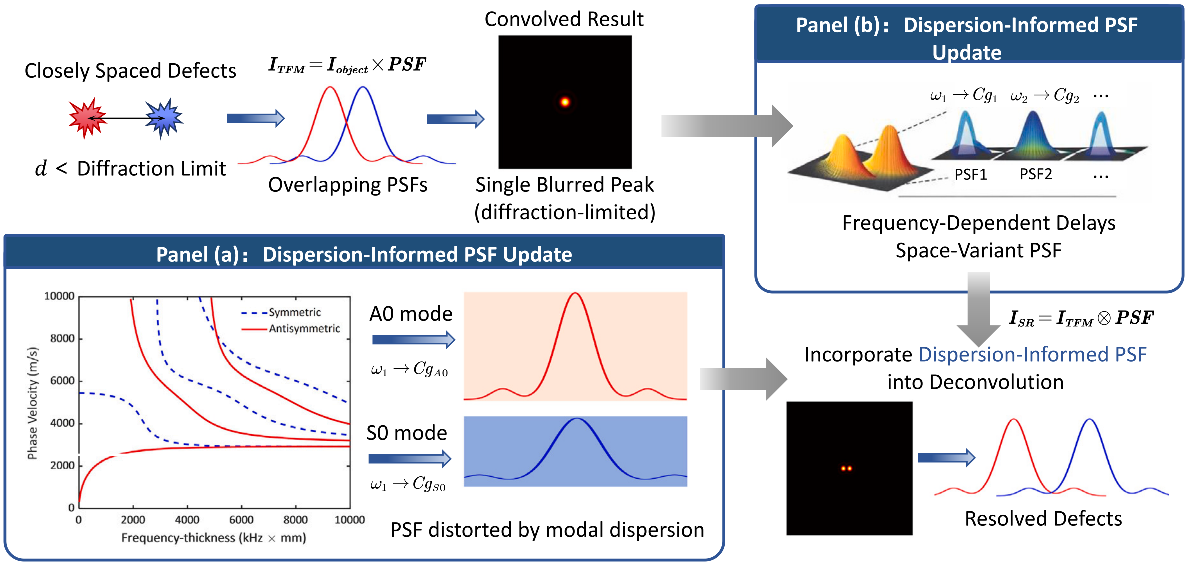

Fig. 1. Schematic illustration of dispersion-informed PSF modeling for Lamb-wave super-resolution imaging. In conventional TFM, the reconstructed image corresponds to the convolution of the true defect distribution with the system PSF, leading to diffraction-limited resolution. For Lamb waves, the PSF is fundamentally shaped by dispersion physics: different propagation modes and frequency-dependent group velocities introduce mode- and frequency-specific arrival distortions, resulting in an intrinsically space-variant PSF. Accurate modeling of this dispersion-informed PSF is therefore essential for physically consistent deconvolution and super-resolution defect separation.

under low signal-to-noise ratio (SNR) conditions [22–25]. These limitations motivate the exploration of alternative super-resolution strategies that are both physically grounded and practically robust.

In this context, as a representative delay-and-sum (DAS) strategy, the Total Focusing Method (TFM) remains a widely adopted beamforming imaging framework in ultrasonic NDT due to its physical transparency, strong noise robustness, and modest hardware requirements [26–30]. By coherently focusing full-aperture array data at every point within the inspection region, TFM provides reliable baseline imaging performance and has been extensively validated in guided-wave inspection scenarios [31,32]. These attributes make TFM an attractive benchmark for further resolution enhancement, provided that its fundamental physical limitations can be properly addressed [26,27]. Unlike these data-driven approaches, the present study seeks super-resolution enhancement through a physics-informed forward model, so that resolution improvement can be achieved in a training-free and physically interpretable manner.

From a physical standpoint, conventional TFM imaging may be interpreted as a forward convolution process, in which the reconstructed image corresponds to the convolution of the true scatterer distribution with the system point spread function (PSF) [33]. The finite mainlobe width and pronounced sidelobes of the PSF inevitably introduce spatial blurring and interference, preventing reliable separation of closely-spaced defects and enforcing the classical diffraction limit [34]. Consequently, improving super-resolution imaging resolution naturally leads to an inverse problem formulation, which is achieved by inverting the PSF-induced blurring.

While *deconvolution*-based techniques have been extensively studied in acoustic and optical source imaging [35–37], their application to ultrasonic Lamb-wave multi-probe array imaging (ULMPAI) presents unique challenges. Unlike air- or water-coupled acoustics, Lamb-wave propagation in solid plates is characterized by strong modal and frequency dispersion [38,39]. These effects render the effective PSF inherently frequency-, mode-, and space-dependent, fundamentally violating the spatial invariance assumptions underlying most conventional deconvolution frameworks. As a result, deconvolution approaches that neglect Lamb-wave dispersion physics are prone to modeling inconsistencies and limited resolution gains in practical NDT scenarios.

To address this challenge, in this study we present a physics-informed deconvolution framework that constructs a dispersion-aware PSF by explicitly accounting for the frequency- and mode-dependent propagation characteristics of Lamb waves, as schematically illustrated in Fig. 1. By incorporating this physically consistent PSF into the TFM forward imaging model, the proposed approach enables a physically interpretable inversion of dispersion-induced blurring in ultrasonic guided-wave imaging. On this basis, the resulting super-resolution imaging problem is efficiently solved using a Lamb-wave-dispersion-aware, FFT-accelerated Fast Iterative Shrinkage-Thresholding Algorithm (FISTA [40,41]), leading to a complete dispersion-informed deconvolution framework termed LWD-FISTA (pipeline in Fig. 2). More importantly, the methodological advance of the present work does not lie in introducing a new generic iterative deconvolution solver, but in improving the PSF itself so that the forward model more faithfully reflects the actual dispersive physics of Lamb-wave propagation. In contrast to existing deconvolution approaches that typically employ a nominal or only weakly physics-informed blur kernel, the proposed framework explicitly embeds Lamb-wave dispersion into PSF construction and the associated imaging operator. Although the Lamb-wave PSF is physically frequency-, mode-, and space-dependent, the present implementation adopts a local shift-invariant approximation within a limited imaging region of interest (ROI), so that a representative dispersion-informed kernel can be used for efficient FFT-based deconvolution. This PSF-level improvement is particularly important for ultrasonic guided-wave imaging, where dispersion-induced model mismatch directly degrades focusing quality and limits defect separability. By reducing this forward-model mismatch, the proposed LWD-FISTA framework enables a more physically consistent deconvolution process for Lamb-wave array imaging and thereby improves the reliability of super-resolution reconstruction for closely spaced defects. The effectiveness of the framework is systematically validated through finite element simulations and laboratory experiments, with further investigations into the influence of aperture size and sensor spacing, and comparative studies against TR-MUSIC under low-SNR conditions. Results and discussions are presented, with challenges identified in this study.

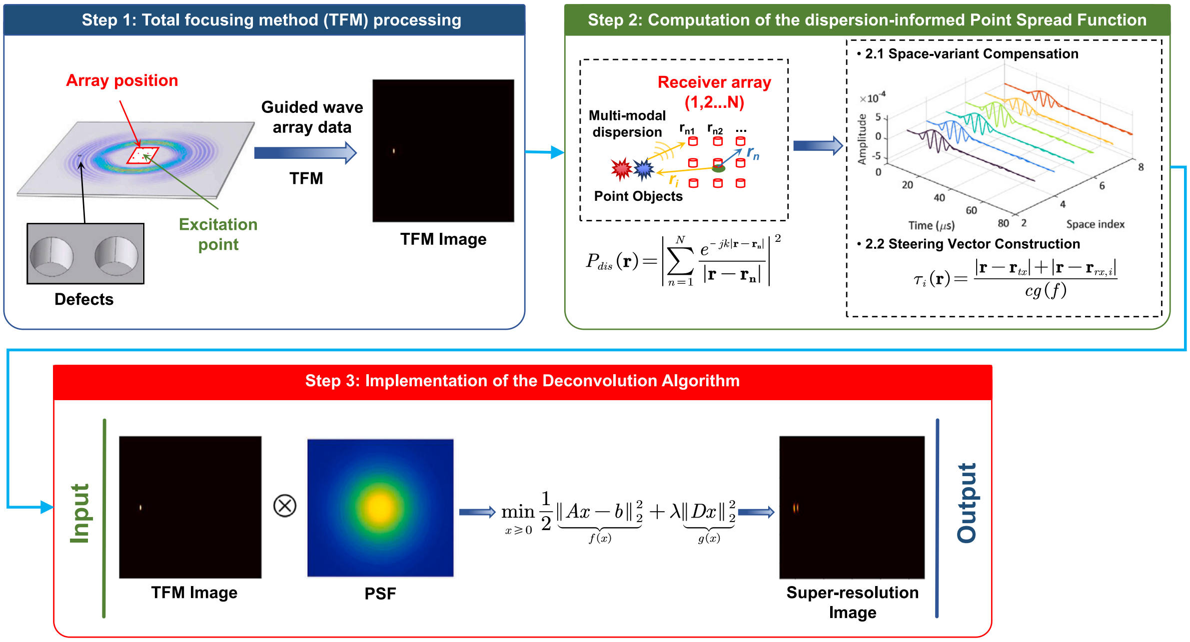

Fig. 2. The proposed framework for the super-resolution algorithm.

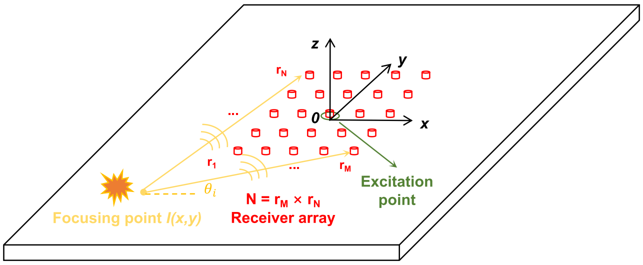

Fig. 3. Illustration of the Total Focusing Method (TFM).

2. Methodology

2.1. Total focusing method (TFM) and imaging resolution

In this work, the TFM is employed as a baseline imaging operator to generate an initial defect map from guided-wave array measurements. As a representative delay-and-sum (DAS) beamforming technique, TFM synthetically focuses the recorded wavefield at each pixel within the region of interest by compensating for the propagation delays between the excitation point, the imaging location, and the receiver array. This full-aperture focusing procedure yields a spatial reflectivity image $I(x,y)$ from the measured Lamb-wave responses.

Fig. 3 illustrates the guided-wave array configuration and the principle of TFM beamforming. For a given imaging pixel (x,y), the recorded signals are time-shifted according to the assumed propagation paths and coherently summed to produce the TFM image,

$$I(x,y) = \left|\sum_{n=1}^{N} h_{ri}\left(\frac{\sqrt{x^2+y^2}+\sqrt{(x_i-x)^2+(y_i-y)^2}}{c_g}\right)\right| \tag{1}$$

where $h_{ri}(t)$ denotes the Lamb-wave response recorded at the nth receiver located at (x_i, y_i), N is the total number of receiver positions, and c_g is the group velocity of the selected guided-wave mode.

Despite its robustness and physical transparency, the spatial resolution of TFM is fundamentally limited by diffraction. Under idealized conditions, the minimum resolvable defect separation is commonly characterized by the Rayleigh criterion,

$$d_R = \frac{0.61\lambda}{\sin\theta_R} \tag{2}$$

where λ is the wavelength and θ_R denotes the effective angular aperture at the imaging point, determined by the array geometry and inspection configuration. This expression reflects the intrinsic spreading of wave energy from a point scatterer due to the finite aperture, resulting in a broadened mainlobe in the system PSF.

More generally, the PSF characterizes the spatial response of the imaging system to an idealized point scatterer and encapsulates the combined effects of wavelength, aperture, array geometry, and propagation physics. Under linear beamforming assumptions, the reconstructed image $I(x,y)$ can be interpreted as the convolution of the true scatterer distribution $\rho(x,y)$ with the system PSF,

$$I(x,y) = \rho(x,y) * \mathrm{PSF}(x,y) \tag{3}$$

where the finite mainlobe width and accompanying sidelobes of the PSF fundamentally govern the achievable imaging resolution. Thus, the Rayleigh criterion may be viewed as a practical manifestation of the PSF mainlobe extent, linking diffraction-limited resolution directly to the shape and spread of the PSF. From this perspective, TFM may be interpreted as a diffraction-limited forward imaging process governed by the PSF. Consequently, achieving resolution beyond this limit requires explicitly counteracting the PSF-induced blurring, which naturally motivates a deconvolution-based formulation introduced in next Section 2.2.

2.2. The Lamb wave dispersion-aware deconvolution algorithm for super-resolution lamb wave imaging

As discussed in Section 2.1, the beamforming process inevitably spreads the energy of a point scatterer over a finite spatial extent, leading to blurred images and poor separability of closely spaced defects. To mitigate this limitation and achieve sharper localization, deconvolution-based strategies have been introduced to explicitly suppress the effect of the PSF.

Within this framework, the TFM beamforming output, commonly referred to as a *dirty map*, which can be interpreted as the convolution

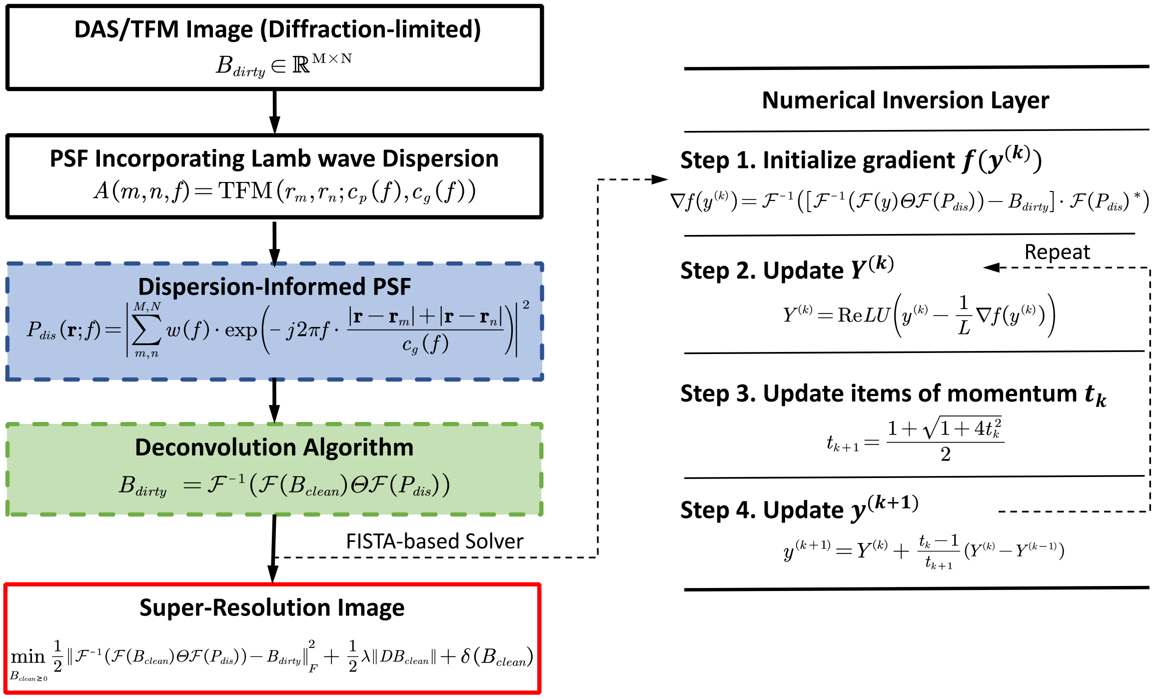

Fig. 4. Algorithmic Workflow of the PSF revised super-resolution deconvolution algorithm.

between the system PSF and an underlying distribution of point-like scatterers. Each point source corresponds to the spatial response of an individual defect, while the PSF characterizes the imaging system's response to a unit-strength point scatterer [42]. Assuming a point source located at position $\boldsymbol{r}_p$, the PSF evaluated at position $\boldsymbol{r}$ can be expressed as

$$\mathrm{PSF}\left(\boldsymbol{r}\middle|\boldsymbol{r}_p\right) = \frac{1}{M^2}\boldsymbol{v}(\boldsymbol{r})^T\left[\boldsymbol{v}_p(\boldsymbol{r}_p)\boldsymbol{v}_p(\boldsymbol{r}_p)^T\right]\boldsymbol{v}(\boldsymbol{r}) \tag{4}$$

where the steering vectors $\boldsymbol{v}_p(\boldsymbol{r}_p)$ and $\boldsymbol{v}(\boldsymbol{r})$ are defined as

$$\boldsymbol{v}_p(\boldsymbol{r}_p) = \left[\frac{|d|}{|d-d_n|}e^{-jk|d-d_n|}\ \cdots\ \frac{|d|}{|d-d_N|}e^{-jk|d-d_N|}\right] \tag{5}$$

$$\boldsymbol{v}(\boldsymbol{r}) = \left[\frac{|d-d_n|}{|d|}e^{-jk|d-d_n|}\ \cdots\ \frac{|d-d_N|}{|d|}e^{-jk|d-d_N|}\right] \tag{6}$$

Here, n ($n = 1, 2, \ldots, N$) denotes the position of the nth array sensor; $|d|$ is the distance from the array center to the beamformer focus; $|d_n|$ is the distance from the array center to the nth sensor; $|d - d_n|$ represents the distance between the focus point and the nth sensor; and k is the wavenumber of the incident Lamb wave.

In conventional deconvolution formulations, the PSF is assumed to be shift-invariant, implying that translating a point scatterer within the imaging domain produces a corresponding translation of the beamforming response without altering its shape [35]. However, unlike acoustic waves in homogeneous fluids, Lamb waves propagate in plate-like structures as multiple dispersive modes whose group velocities depend strongly on frequency and propagation direction. As a result, the effective PSF associated with TFM imaging becomes inherently frequency-, mode-, and space-dependent, posing a fundamental challenge to physically consistent deconvolution.

To overcome this limitation, we formulate a dispersion-informed deconvolution framework in which the Lamb-wave dispersion physics is explicitly embedded into the PSF modeling. Rather than treating the PSF as an idealized, stationary kernel, the proposed approach constructs a physically consistent PSF that accounts for frequency-dependent group velocity, modal characteristics, and geometric spreading effects. This dispersion-aware PSF provides an accurate forward imaging model for Lamb-wave TFM and forms the foundation for super-resolution reconstruction.

Under this formulation, the present study incorporates Lamb-wave dispersion into PSF modeling, leading to a dispersion-informed PSF, denoted as P_{dis}, which explicitly accounts for the frequency- and mode-dependent propagation characteristics of guided waves. As a result, the conventional shift-invariant deconvolution formulation in Eq. (3) is accordingly reformulated, yielding the dispersion-informed deconvolution model given in Eq. (7), following the framework of Ehrenfried and Koop [38] as

$$B_{dirty} = B_{clean} * P_{dis} + n(0, \sigma^2) \tag{7}$$

where B_{clean} represents the ideal reflectivity map (ground truth), B_{dirty} denotes the measured beamforming image, P_{dis} is the PSF evaluated at the center of the imaging domain, and $*$ denotes convolution. To stabilize the inversion, measurement noise is commonly modeled as additive Gaussian noise, and prior information is incorporated by enforcing non-negativity of the beamforming power.

Using the convolution theorem, Eq. (7) can be efficiently reformulated in the frequency domain as

$$B_{dirty} = \mathcal{F}^{-1}\left(\mathcal{F}\left(B_{clean}\right)\Theta\mathcal{F}\left(P_{dis}\right)\right) \tag{8}$$

where $\mathcal{F}(\cdot)$ and $\mathcal{F}^{-1}(\cdot)$ denote the two-dimensional fast Fourier transform (2D-FFT) and its inverse (2D-iFFT), respectively, and Θ represents the Hadamard product [43]. In this formulation, the PSF P_{dis} acts as a discrete blurring operator, and recovering B_{clean} from B_{dirty} constitutes a classical ill-posed inverse problem [44]. Consequently, the objective of deconvolution in this study is not to perfectly recover the true defect distribution, but to obtain a physically consistent and stable estimate of B_{clean} that best explains the measured beamforming map under the constraints imposed by the imaging system. This highlights the dual importance of (i) constructing an accurate, dispersion-informed PSF that faithfully represents the system response, and (ii) employing a regularized optimization framework to stabilize the inversion and suppress non-physical solutions. The detailed numerical implementation, including the FFT-FISTA solver and convergence considerations, is provided in Appendix. Accordingly, the dispersion-informed deconvolution problem is cast as a regularized optimization model and solved using an FFT-accelerated FISTA scheme, leading to the formulation given in Eq. (9):

$$\min_{B_{clean}\geq 0} \frac{1}{2}\left\|\mathcal{F}^{-1}\left(\mathcal{F}\left(B_{clean}\right)\Theta\mathcal{F}\left(P_{dis}\right)\right)-B_{dirty}\right\|_F^2 + \frac{\alpha}{2}\left\|D\cdot B_{clean}\right\|_F^2+\delta\left(B_{clean}\right) \tag{9}$$

where D denotes a first-order difference operator that promotes spatial regularity, α is a regularization parameter, and the non-negativity constraint $\delta(\cdot)$ reflects the physical nature of defect reflectivity.

The central element of this formulation is the construction of the dispersion-informed PSF. In the context of Lamb-wave TFM imaging, the PSF represents the beamformer response to an idealized unit-strength point scatterer. For a reference scatterer located at $\mathbf{r}_0$, the PSF evaluated at an arbitrary imaging point $\mathbf{r}$ is modeled by explicitly preserving the dispersive phase accumulation associated with frequency-dependent group velocity,

$$P_{dis}(\mathbf{r};f) = \left|\sum_{n=1}^{N} w(f)\,\exp\left(-j2\pi f\,\frac{|\mathbf{r}-\mathbf{r}_n|+|\mathbf{r}-\mathbf{r}_i|}{c_g(f)}\right)\right|^2 \tag{10}$$

where $\mathbf{r}_n$ denotes the position of the nth receiver, $w(f)$ is a frequency weighting window, and $c_g(f)$ is the frequency-dependent group velocity of the selected Lamb-wave mode. In practical Lamb-wave measurements, the recorded wavefield may contain multiple propagating modes simultaneously. The measured signal can therefore be written as

$$u(\mathbf{r},t)=\sum_{m=1}^{M}u_m(\mathbf{r},t)+n(\mathbf{r},t) \tag{11}$$

where $u_m(\mathbf{r},t)$ denotes the contribution of the mth Lamb-wave mode and $n(\mathbf{r},t)$ represents measurement noise. In the present work, deconvolution is performed for a selected target mode q, whose dispersion relation is either known theoretically or pre-characterized experimentally.

To extract the target mode from mixed-mode measurements, the full wavefield is first transformed into the wavenumber–frequency domain:

$$U(\mathbf{k},\omega)=\mathcal{F}_{\mathbf{r},t}\{u(\mathbf{r},t)\} \tag{12}$$

A dispersion-guided modal filter is then constructed around the target-mode branch $k_q(\omega)$,

$$W_q(\mathbf{k},\omega)=\exp\left[-\frac{\left(|\mathbf{k}|-k_q(\omega)\right)^2}{2\sigma_q^2}\right] \tag{13}$$

so that the target-mode component can be extracted as

$$U_q(\mathbf{k},\omega)=W_q(\mathbf{k},\omega)\,U(\mathbf{k},\omega) \tag{14}$$

$$u_q(\mathbf{r},t)=\mathcal{F}^{-1}_{\mathbf{k},\omega}\{U_q(\mathbf{k},\omega)\} \tag{15}$$

The subsequent PSF construction and deconvolution are therefore performed for the selected mode q, rather than for the raw mixed-mode signal itself. Accordingly, the imaging model can be written as

$$y_q=A_q x+\varepsilon_q \tag{16}$$

where A_q is the forward operator constructed from the target-mode dispersion relation, and ε_q collects residual modal leakage, imperfect mode separation, and measurement noise. This formulation implies that modal coexistence does not alter the definition of the target-mode PSF itself; instead, insufficient mode separation appears as a residual term in the inversion model. Therefore, as long as the target-mode component can be sufficiently extracted, or remains dominant within the selected frequency–wavenumber region, the same target-mode PSF remains valid for deconvolution.

It should be noted that the present study focuses on mode-selected Lamb-wave imaging, and the current validation is performed separately for the S_0 and A_0 modes. More challenging cases involving severe multimode overlap or strongly anisotropic propagation are beyond the scope of the present manuscript and will require further extension of the forward model.

The PSF is obtained by synthesizing the TFM response to a point scatterer $\mathbf{r}_0$ and normalized to ensure numerical stability. The corresponding steering and excitation vectors are defined as

$$h_n(\mathbf{r})=\frac{|\mathbf{r}_0-\mathbf{r}_n|}{|\mathbf{r}-\mathbf{r}_n|}\cdot\exp\left(-j\omega\frac{|\mathbf{r}-\mathbf{r}_n|}{c_g(f)}\right) \tag{17}$$

$$e_n(\mathbf{r})=\frac{|\mathbf{r}-\mathbf{r}_n|}{|\mathbf{r}_0-\mathbf{r}_n|}\cdot\exp\left(-j\omega\frac{|\mathbf{r}_0-\mathbf{r}_n|}{c_g(f)}\right) \tag{18}$$

The PSF at location $\mathbf{r}$ is then computed as the normalized TFM output

$$P_{dis}(\mathbf{r})=\left|\sum_{n=1}^{N}h_n(\mathbf{r})\cdot\mathbf{e}_n^*\right|^2/N^2 \tag{19}$$

where $\mathbf{e}_n^*$ denotes complex conjugation. This matched-filter-based PSF construction naturally incorporates both modal dispersion and spatial variability, yielding a physically faithful representation of the Lamb-wave imaging system. By embedding this dispersion-informed PSF into the forward imaging model, the proposed framework enables meaningful deconvolution that explicitly counteracts diffraction- and dispersion-induced blurring. The overall dispersion-informed deconvolution workflow is summarized in Fig. 4.

The focused image can be written as

$$y(\mathbf{r})=\int_{\Omega}P_{dis}(\mathbf{r},\xi)\,x(\xi)\,d\xi+n(\mathbf{r}) \tag{20}$$

where $P_{dis}(\mathbf{r},\xi)$ denotes the space-dependent PSF associated with an observation point $\mathbf{r}$ and a reflector location ξ. Therefore, the full physical model is not strictly shift-invariant.

However, the present study considers a limited imaging ROI, within which the spatial variation of the PSF is assumed to be moderate after target-mode selection and dispersion-informed correction. Under this condition, a local shift-invariant approximation is adopted for computational tractability. Specifically, with respect to a reference point $\mathbf{r}_c$ (taken as the ROI center in the present implementation), the PSF is approximated as

$$P_{dis}(\mathbf{r},\xi)\approx P_{\mathbf{r}_c}(\mathbf{r}-\xi),\qquad \mathbf{r},\xi\in\Omega_{\mathrm{ROI}} \tag{21}$$

so that the imaging model becomes

$$y(\mathbf{r})\approx\int_{\Omega_{\mathrm{ROI}}}P_{\mathbf{r}_c}(\mathbf{r}-\xi)\,x(\xi)\,d\xi+n(\mathbf{r}) \tag{22}$$

where $P_{\mathbf{r}_c}$ is the representative dispersion-informed PSF operator evaluated at the reference location. The FFT acceleration used in Eq. (7) is therefore applied to this *local shift-invariant approximation*, rather than to the full globally space-variant PSF.

3. Numerical validation on sub-diffraction-limit imaging

3.1. Finite element validation of sub-diffraction-limit imaging

In this section, the proposed super-resolution framework is validated through finite element simulations designed to emulate sub-diffraction-limit defect imaging scenarios. The primary objective is to quantitatively assess the ability of the proposed LWD-FISTA algorithm to overcome the intrinsic resolution limitations of conventional TFM.

Finite element simulations are conducted using COMSOL Multiphysics 6.0, and the overall simulation configuration is illustrated in Fig. 5. The model consists of an aluminum plate with dimensions of 600 mm × 600 mm and a thickness of 4 mm. Guided waves are excited on the back surface of the plate using a five-cycle Hanning-windowed tone burst with a central frequency of 200 kHz. A synthetic sensor array is deployed over a 100 mm × 100 mm region centered on the front

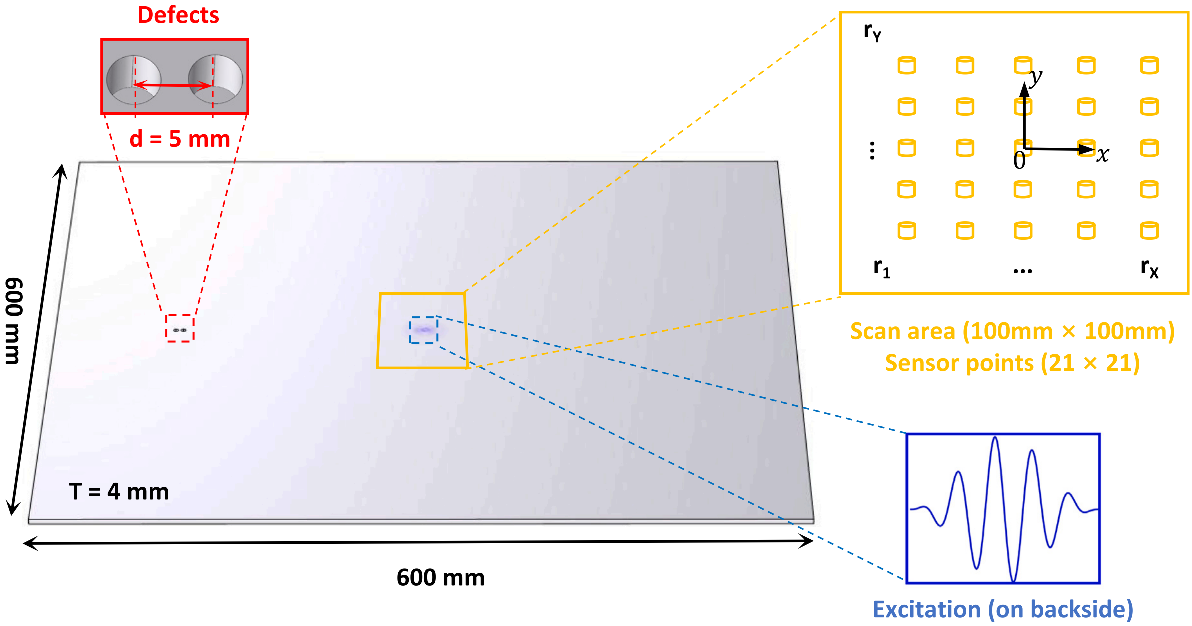

Fig. 5. Ultrasonic phased array simulation system. There are two hole defects with a distance of 5 mm. The shortest wavelength of the incident wave is 14 mm (corresponding to wavelength of A_0 mode). According to Rayleigh's half-wavelength criterion, the distance of 5 mm is smaller than the diffraction limit 7 mm. Thus super-resolution algorithms and advanced ultrasonic imaging are necessary to identify these two defects.

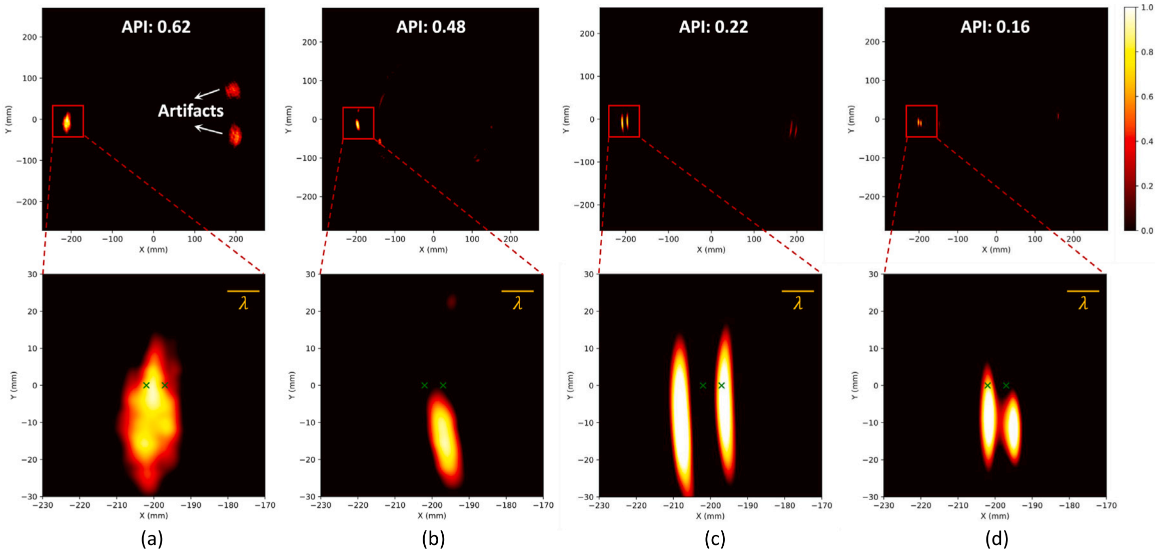

Fig. 6. (a) and (b) represent the traditional TFM results using different modes to detect defects, (a) using only the S_0 mode and (b) using only the A_0 mode, both failing to identify the sub-diffraction-limit spaced defects; (c) and (d) represent the LWD-FISTA results using different modes to detect defects, (c) using only the S_0 mode and (d) using only the A_0 mode, both identifying the sub-diffraction-limit spaced defects. The aperture size is 100 mm and sensor spacing is 5 mm. The green markers indicate the ground-truth defect locations for reference. API (array performance indicator) is defined as the −6 dB mainlobe area of the effective PSF normalized by λ^2; a smaller value indicates a more compact PSF and higher spatial resolution. (For interpretation of the references to colour in this figure legend, the reader is referred to the web version of this article.)

surface of the plate, with an inter-element spacing of 5 mm. To simulate closely-spaced defects, two circular holes with a radius of 1 mm and a depth of 2 mm are introduced at a location 100 mm from the left boundary of the plate, with a center-to-center separation of 5 mm.

The present study defines the reference resolution limit as the diffraction-limited (Rayleigh half-wavelength criterion) baseline of conventional TFM under the same acquisition configuration. In the 200 kHz, 4 mm aluminum-plate case considered here, the dominant wavelengths are approximately 28 mm for the S_0 mode and 14 mm for the A_0 mode, corresponding to diffraction-limited baselines on the order of 14 mm and 7 mm, respectively. Therefore, for the present defect configuration with a center-to-center spacing of 5 mm, the separation task lies below the conventional TFM diffraction-limited baseline in the A_0 dominated case. In this sense, the term *super-resolution* in this work is used operationally to indicate resolution beyond the conventional TFM diffraction limit under the same aperture and sensor configuration.

This limitation is clearly observed in the conventional TFM (representative results are shown in Fig. 6(a) and (b)). Neither the S_0 nor the A_0 mode is able to distinctly resolve the two circular holes, and the reconstructed images exhibit a single blurred response due to diffraction-induced energy spreading. Interestingly, while both modes fail to achieve defect separation, the A_0 mode yields comparatively

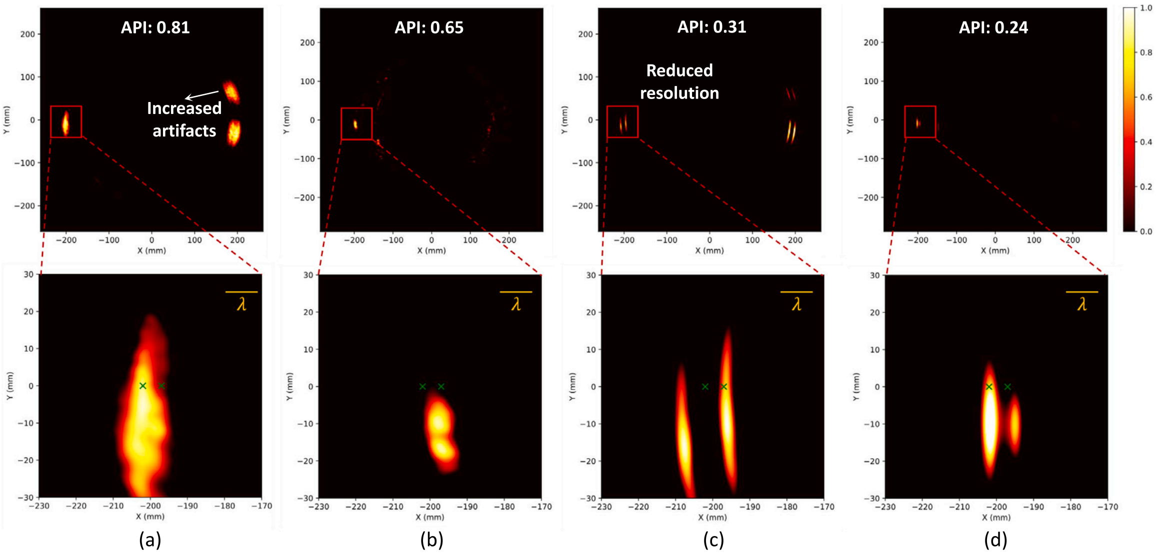

Fig. 7. (a) and (b) represent the traditional TFM results using different modes to detect defects: (a) using only the S_0 mode and (b) using only the A_0 mode, both failing to identify the sub-diffraction-limit spaced defects. (c) and (d) represent the LWD-FISTA results using different modes to detect defects: (c) using only the S_0 mode and (d) using only the A_0 mode, both identifying the sub-diffraction-limit spaced defects. The aperture size is 80 mm (**reduced**) while fixed sensor spacing of 5 mm. The green markers indicate the ground-truth defect locations for reference. (For interpretation of the references to colour in this figure legend, the reader is referred to the web version of this article.)

improved localization performance owing to its shorter wavelength, which leads to a narrower effective PSF. In contrast, the proposed LWD-FISTA method successfully resolves the two sub-diffraction-limit defects (Fig. 6(c) and (d)), where the magnified views clearly demonstrate accurate separation and localization of the two closely-spaced holes. Both the S_0 and A_0 modes are observed to achieve super-resolution imaging using the proposed framework. These results indicate that LWD-FISTA is able to effectively overcome the diffraction-induced limitations inherent in conventional TFM. Quantitative evaluation using the array performance indicator (API) [2] where a smaller API value indicates a more spatially confined energy distribution, further confirms the superior resolution achieved by the proposed method, reflecting a contracted effective PSF and reduced diffraction-induced spreading.

The distinct difference between the conventional TFM result and the proposed method may be directly attributed to the underlying PSF structure. In the conventional TFM image, the two closely-spaced defects fall within the effective mainlobe width of the PSF and are therefore merged into a single blurred response, consistent with diffraction-limited behavior. In contrast, by explicitly incorporating Lamb-wave dispersion into PSF modeling and inversion, the proposed approach effectively suppresses sidelobe interference and contracts the effective mainlobe, enabling the two defects to be clearly resolved.

Importantly, the observed resolution enhancement is not a numerical artifact of the inverse solver, but a direct consequence of physically consistent PSF reconstruction. By accounting for mode- and frequency-dependent spatial spreading, the dispersion-informed PSF accurately captures the true imaging system response, ensuring that the recovered defect separation reflects the underlying guided-wave scattering physics.

These finite element results confirm that super-resolution in Lamb-wave TFM imaging is fundamentally governed by the structure of the PSF, rather than by post-processing alone. This observation naturally motivates a systematic investigation of the key physical and acquisition parameters that shape the PSF, including aperture size and sensor spacing, which are examined and presented in the following sections.

3.2. *Influence of aperture size on imaging performance*

In this subsection, the influence of array aperture size on the performance of the proposed LWD-FISTA framework is investigated. From the diffraction theory, the lateral resolution of a beamforming-based imaging system scales inversely with its effective aperture: a smaller aperture corresponds to reduced angular coverage, which in turn broadens the mainlobe of the system PSF and elevates sidelobe levels. As a result, aperture size imposes a fundamental physical constraint on the system's ability to resolve closely-spaced defects, independent of the post-processing algorithm employed.

To examine the robustness of the proposed super-resolution approach under aperture-limited conditions, the scanning aperture is reduced from 100 mm to 80 mm while keeping the sensor spacing fixed at 5 mm, as illustrated in Fig. 5. All other simulation parameters are identical to those described in Section 3.1. The reconstructed images for the S_0 and A_0 Lamb-wave modes are presented in Fig. 7, enabling a direct comparison between conventional TFM and the proposed LWD-FISTA under reduced aperture coverage.

The conventional TFM reconstructions obtained with the reduced aperture are shown in Fig. 7(a) and (b). For the S_0 mode, a pronounced increase in sidelobe artifacts is observed, accompanied by severe degradation in defect separability. Physically, this phenomenon arises from the diminished angular aperture of the array, which broadens the effective PSF and weakens the suppression of off-axis energy contributions, thereby amplifying imaging artifacts and blurring the defect responses.

In parallel the LWD-FISTA reconstructions are shown in Fig. 7(c) and (d). Although a noticeable reduction in overall image sharpness is observed compared with the *full*-aperture case, the two adjacent defects remain resolvable for both Lamb-wave modes, indicating the proposed method retains its super-resolution capability even when the available spatial aperture is reduced. The observed degradation in sharpness can be attributed to the inherent loss of spatial bandwidth associated with the smaller aperture, which limits the highest recoverable spatial frequencies, even after deconvolution.

Discussion: Overall, these results indicate the robustness of the proposed LWD-FISTA framework. From a physical perspective, aperture reduction primarily affects the angular diversity of the measured wavefield and therefore limits the spatial bandwidth available for imaging. The results presented here indicate that, within the considered aperture configuration, sufficient wavefield diversity is preserved to support physically consistent PSF inversion and super-resolution reconstruction. These observations suggest that, while aperture size governs the

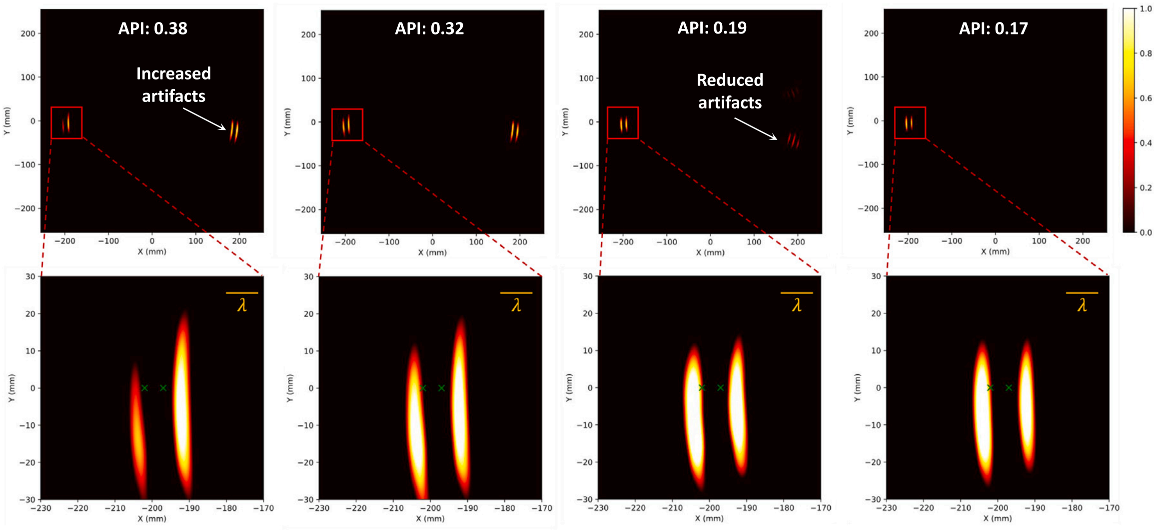

(a) (b) (c) (d)

Fig. 8. The LWD-FISTA image of only using S_0 mode of different sensor spacing while a fixed aperture size of 100 mm. Sensor spacing: (a) 10 mm, (b) 8 mm, (c) 2.5 mm and (d) 2 mm.

angular content of the PSF, the fidelity of super-resolution imaging also critically depends on how well the wavefield is spatially sampled, which motivates the following investigation into the influence of sensor spacing.

3.3. The effect of sensor spacing

In this section, the influence of sensor spacing on the super-resolution performance of the proposed LWD-FISTA framework is investigated. While the aperture size determines the angular coverage of the array, the sensor spacing governs the spatial sampling density of the measured wavefield, thereby directly affecting the recoverable spatial bandwidth and the conditioning of the inverse problem. Varying the sensor spacing therefore provides a critical insight into the trade-off between measurement effort and achievable imaging performance.

To isolate this effect, the scanning aperture is fixed at 100 mm, while the sensor spacing is varied among 10 mm, 8 mm, 2.5 mm, and 2 mm, as illustrated in Fig. 8. This configuration enables a controlled comparison between spatially undersampled and densely sampled array measurements.

The imaging results obtained with coarse sensor spacings of 10 mm and 8 mm, respectively, are shown in Fig. 8(a) and (b). A noticeable degradation in image quality is observed, characterized by elevated sidelobe levels, increased artifacts, and blurred defect signatures. From a physical perspective, such degradation arises from spatial undersampling of the Lamb-wave field, which limits the capture of high-spatial-frequency components and introduces aliasing effects. Consequently, the system PSF becomes poorly defined, undermining both conventional beamforming and subsequent deconvolution.

In contrast, the reconstructions obtained with reduced sensor spacings of 2.5 mm and 2 mm are shown in Fig. 8(c) and (d). In these cases, the two closely-spaced defects are clearly resolved with minimal sidelobe interference and improved localization accuracy. Dense spatial sampling enables a more faithful representation of the guided-wave field, effectively increasing the usable spatial bandwidth of the array and yielding a well-conditioned PSF. This, in turn, provides a stable foundation for the sparsity-promoting deconvolution in LWD-FISTA, allowing super-resolution features to be reliably recovered.

Discussion: It should be noted, however, that finer sensor spacing inevitably increases both data acquisition and computational costs. For example, reducing the spacing from 5 mm to 2 mm increases the number of sensing points from 441 to 2601 within the same aperture. This highlights the practical necessity of balancing imaging performance against measurement efficiency.

From a theoretical standpoint, the selection of sensor spacing is fundamentally constrained by the spatial Nyquist sampling criterion, which requires the sampling interval to be smaller than half of the shortest wavelength of interest to avoid aliasing and preserve wavefield fidelity. Adequate spatial sampling is therefore essential not only for conventional TFM imaging, but also for ensuring the stability and effectiveness of deconvolution-based super-resolution methods. Excessively coarse spacing leads to irreversible information loss that cannot be compensated by post-processing, whereas sufficiently dense sampling enables accurate mode representation, robust PSF inversion, and reliable subwavelength defect imaging.

3.4. Robustness to noise: comparison with TR-MUSIC

In this section, the sub-diffraction-limit imaging performance of the proposed LWD-FISTA algorithm is evaluated in comparison with a widely adopted super-resolution technique, TR-MUSIC. TR-MUSIC exploits the orthogonality between signal and noise subspaces to achieve fine defect localization beyond the classical diffraction limit and has been extensively reported for high-resolution ultrasonic imaging. By benchmarking against TR-MUSIC under varying SNR conditions, we aim to assess not only the achievable resolution of both methods but also their robustness and practical reliability in noise-contaminated environments.

A fundamental distinction between the two approaches lies in their array configurations and data requirements. TR-MUSIC typically relies on a multi-input multi-output (MIMO) array to construct a full multistatic response matrix, enabling accurate subspace decomposition at the expense of increased system complexity and data acquisition cost. In contrast, the proposed LWD-FISTA framework operates under a single-input multiple-output (SIMO) configuration, which significantly reduces hardware and acquisition demands. It should be noted that the comparison between TR-MUSIC and the proposed LWD-FISTA is not intended as a strictly configuration-matched head-to-head benchmark. Classical TR-MUSIC is typically formulated using multistatic response data and is therefore implemented here under a MIMO acquisition setting, whereas the proposed method operates in a SIMO framework. Accordingly, the purpose of this comparison is not to claim absolute superiority under identical information content, but to contrast the practical imaging performance and acquisition requirements of two

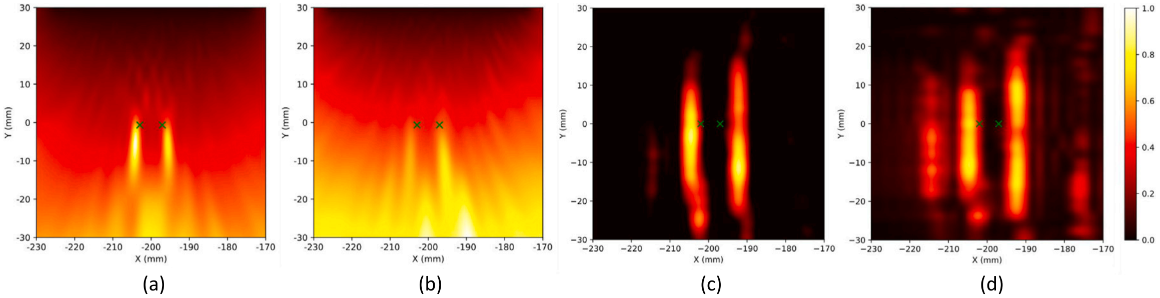

Fig. 9. The TR-MUSIC results of different SNR (a) 5 dB and (b) 0 dB. The LWD-FISTA results of different SNR (c) 5 dB and (d) 0 dB.

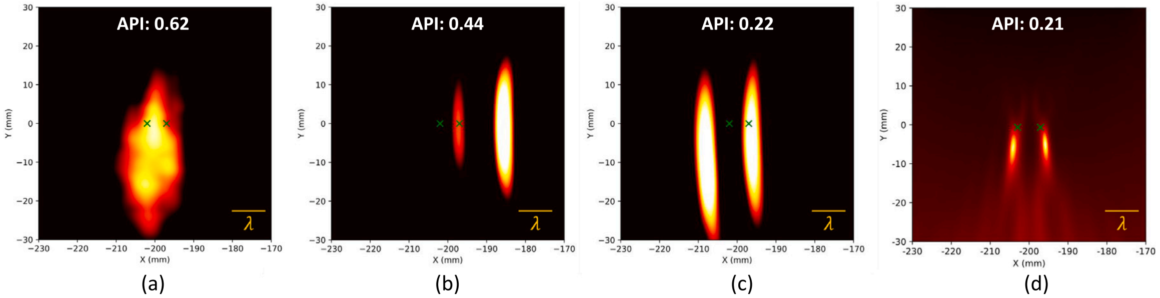

Fig. 10. Ablation study on the same dataset under an SNR of 30 dB. (a) Conventional TFM; (b) conventional deconvolution using a nominal PSF without dispersion embedding; (c) the proposed dispersion-informed deconvolution (LWD-FISTA); and (d) TR-MUSIC. In (b) and (c), the same FISTA solver, regularization form, and convergence settings are used, so that the only difference lies in the PSF model.

representative super-resolution strategies under their standard operating conditions. Moreover, because the MIMO configuration provides TR-MUSIC with richer measurement information than the SIMO setting used by LWD-FISTA, the comparison should be interpreted as a practical benchmark of robustness and deployability rather than a comparison that artificially favors the proposed method.

The TR-MUSIC reconstructions at SNR levels of 5 dB and 0 dB, respectively, are presented in Fig. 9(a) and (b). At moderate SNR (5 dB), TR-MUSIC successfully resolves the two closely-spaced defects with high localization accuracy, demonstrating its strong super-resolution capability under favorable measurement conditions. However, when the SNR is reduced to 0 dB, the TR-MUSIC image deteriorates markedly, exhibiting pronounced spurious peaks and a loss of defect separability. This degradation arises from the sensitivity of the signal-noise subspace separation to noise contamination, which corrupts the covariance matrix estimation and destabilizes the identification of the signal subspace.

In contrast, the corresponding reconstructions using the proposed LWD-FISTA algorithm under identical noise conditions are shown in Fig. 9(c) and (d). Notably, even at 0 dB SNR, the two defects remain clearly resolved, with well-localized peaks and minimal noise-induced artifacts. This enhanced robustness can be attributed to the physics-informed deconvolution framework, in which the dispersion-corrected PSF of Lamb wave propagation is explicitly embedded into the reconstruction model. By enforcing consistency with the underlying wave physics, the algorithm effectively suppresses incoherent noise contributions and concentrates energy at the true scatterer locations, thereby preserving localization accuracy in severely noisy data. These results emphasize that super-resolution performance in guided-wave imaging should be evaluated not only in terms of theoretical resolution limits, but also in terms of robustness and physical consistency under realistic noise conditions.

Discussion: From a physical standpoint, TR-MUSIC is a purely data-driven subspace method that relies on accurate estimation of the data covariance matrix. When noise power becomes comparable to signal power, perturbations in the covariance matrix can significantly distort the signal subspace, leading to false peaks and unstable imaging results. In contrast, the proposed LWD-FISTA approach leverages a deterministic forward model through the PSF and incorporates regularization to constrain the solution space. This model-based formulation inherently stabilizes the inverse problem, improves the effective image-domain SNR, and mitigates noise-induced artifacts.

3.5. Ablation study on the role of dispersion-informed PSF modeling

To further clarify the source of the performance improvement, an ablation study was carried out on the same dataset under an SNR of 30 dB. Four representative reconstructions are compared side by side: (i) conventional TFM, (ii) conventional deconvolution using a nominal PSF without dispersion embedding, (iii) the proposed dispersion-informed deconvolution (LWD-FISTA), and (iv) TR-MUSIC. For a fair comparison, the deconvolution methods in (ii) and (iii) use the same FISTA solver, the same regularization form, and the same convergence settings. In this way, the influence of the forward-model construction can be separated from that of the numerical optimizer. In other words, the nominal PSF corresponds to a dispersion-frozen kernel, while the proposed PSF is dispersion-informed through the full selected-mode relation $c_g(f)$.

The comparison results are summarized in Fig. 10. As expected, conventional TFM remains diffraction-limited and produces a broadened response in which the two closely spaced defects are not clearly separated. Conventional deconvolution with the nominal PSF provides only limited sharpening relative to TFM. This indicates that using the iterative solver alone is not sufficient when the forward blur kernel does not correctly reflect the dispersive propagation physics of Lamb waves. By contrast, the proposed dispersion-informed deconvolution yields the sharpest reconstruction and the clearest separation of the two defects, demonstrating that the dominant performance gain arises from the physically matched PSF model rather than from the iterative optimization procedure.

For completeness, TR-MUSIC is also included as a representative super-resolution benchmark. It provides high-resolution imaging under

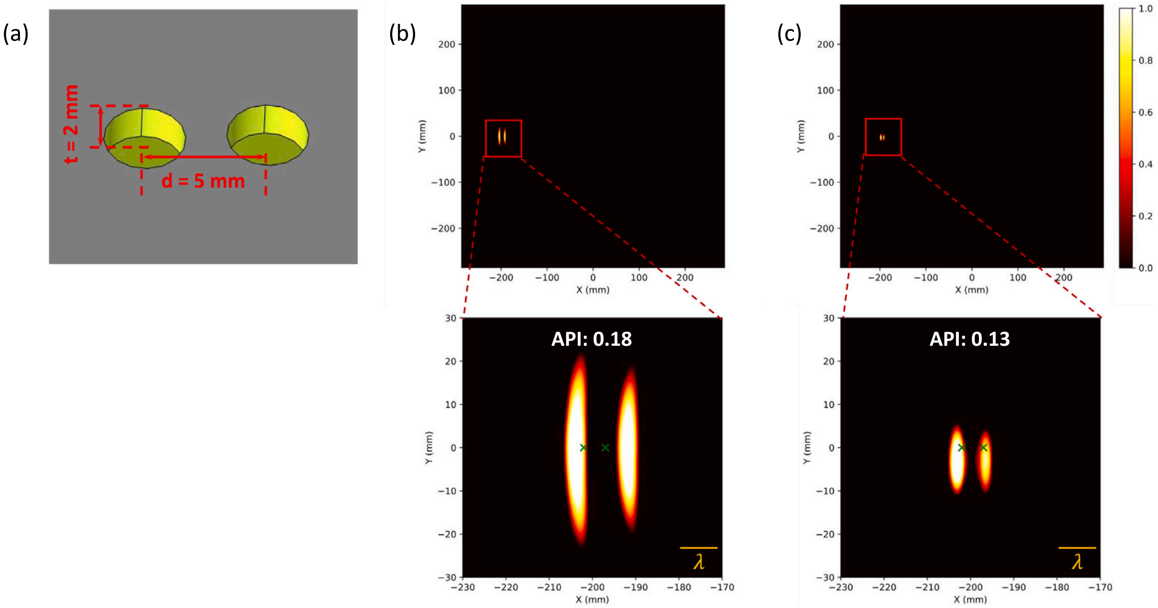

Fig. 11. Finite-element validation on a non-penetrating defect. (a) Schematic of the blind-hole configuration with a depth of 2 mm, while all other simulation conditions remain unchanged from the previous case; (b) super-resolution imaging result for the S_0 mode; and (c) result for the A_0 mode. The results show that the proposed dispersion-informed deconvolution framework remains effective for a non-penetrating defect configuration, indicating that its benefit is not restricted to the idealized through-hole benchmark alone.

favorable conditions, but it is based on a different acquisition paradigm and therefore serves here as a reference super-resolution method rather than as a strictly solver-matched counterpart.

3.6. Finite-element validation on a non-penetrating defect

To further assess the robustness of the proposed framework beyond the 1 mm through-hole benchmark, an additional finite-element study was conducted on a non-penetrating defect configuration. In this example, all simulation conditions were kept unchanged from the previous case, except that the defect was replaced by a blind hole with a depth of 2 mm. The corresponding schematic is shown in Fig. 11(a).

The super-resolution imaging results for this blind-hole case are shown in Fig. 11(b) and (c) for the S_0 and A_0 modes, respectively. It can be observed that the proposed method remains capable of producing a spatially concentrated reconstruction for both modes, indicating that the dispersion-informed PSF inversion is not restricted to the idealized through-hole configuration alone.

It is worth noting that the group velocity used in the dispersion-informed PSF is jointly determined by the excitation frequency and the plate thickness, i.e. $c_g(fd)$. Therefore, uncertainty in either the selected-mode dispersion relation or the nominal thickness directly perturbs the propagation delay embedded in the PSF, and thus appears as a PSF mismatch problem. In the present study, this effect is mitigated by the use of a narrowband excitation and a nominally uniform 4 mm plate, for which the target-mode dispersion relation remains well defined over the imaging region. To further examine the robustness boundary of the proposed method, a sensitivity study was carried out by perturbing the assumed S_0 mode group velocity by ±2% and ±5% relative to the theoretical value.

The corresponding sensitivity results are shown in Fig. 12, where the assumed S_0 mode group velocity is perturbed by −5%, −2%, +2%, and +5%, respectively. It can be observed that moderate perturbations of ±2% introduce only limited degradation in the reconstructed image: the main effect is a mild broadening of the reconstructed peaks together with a slight reduction in focusing sharpness. When the perturbation increases to 5%, the PSF mismatch becomes more evident, leading to stronger peak broadening, reduced contrast, and a more noticeable localization bias. Nevertheless, the degradation remains gradual rather than catastrophic, indicating that the proposed framework is reasonably robust to moderate uncertainty in the assumed group velocity. From a physical point of view, this is because an error in c_g mainly perturbs the delay law embedded in the PSF, and the resulting mismatch is partially absorbed by the sparsity-regularized inversion. Since the Lamb-wave dispersion relation is thickness-dependent, the above sensitivity study also provides a physically relevant indication of how moderate thickness uncertainty may affect the proposed PSF-based reconstruction. In other words, thickness error enters the model primarily through dispersion mismatch, which perturbs the delay consistency of the PSF and gradually degrades super-resolution performance.

4. Experimental validation

Laboratory experimental validation was conducted to further assess the performance and robustness of the proposed LWD-FISTA framework under realistic measurement conditions. The experiments were designed to validate the algorithm's ability to achieve sub-diffraction-limit imaging in guided-wave inspections and to examine its sensitivity to key experimental parameters.

A T6061 aluminum plate with dimensions of 600 mm × 600 mm × 4 mm was selected as the test specimen (Fig. 13). Two circular through-holes with a radius of 1 mm were introduced near the central region of the plate to emulate closely-spaced defects. The holes were separated by a center-to-center distance of $d = 5$ mm and positioned approximately 70 mm away from the reference point. A five-cycle Hanning-windowed sinusoidal tone burst with a central frequency of 200 kHz was employed as the excitation signal. The excitation was applied using a surface-bonded piezoelectric (PZT) transducer mounted at the center of the plate's front surface. Out-of-plane displacement responses within the region of interest were acquired using a Polytec Qtec 3D PSV-500 scanning laser Doppler vibrometer (LDV), operating at a sampling frequency of 5.12 MHz.

Using the experimentally measured S_0 mode Lamb wave responses, the proposed LWD-FISTA method is observed to detect and locate the two closely-spaced defects successfully, as shown in Fig. 14. The reconstructed defect locations exhibit good agreement with the ground-truth positions, with localization errors remaining within acceptable

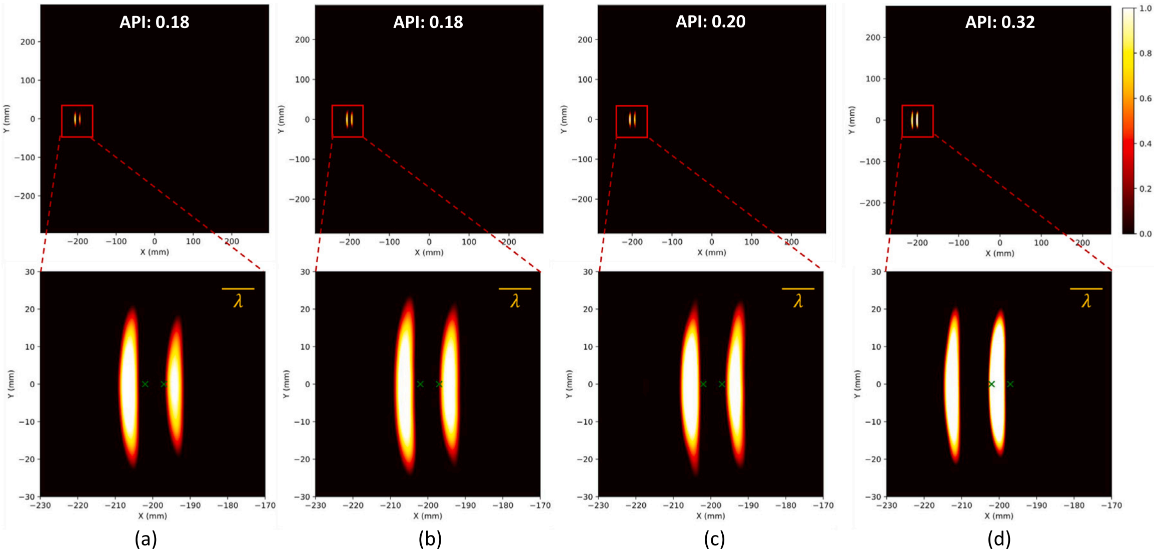

Fig. 12. Sensitivity of the proposed LWD-FISTA reconstruction to uncertainty in the assumed S_0 mode group velocity. The theoretical S_0 mode group velocity at 200 kHz in the 4 mm aluminum plate is approximately 5600 m/s. Panels (a)–(d) show the reconstruction results obtained with perturbed group velocities of (a) −5%, (b) −2%, (c) +2%, and (d) +5%, respectively.

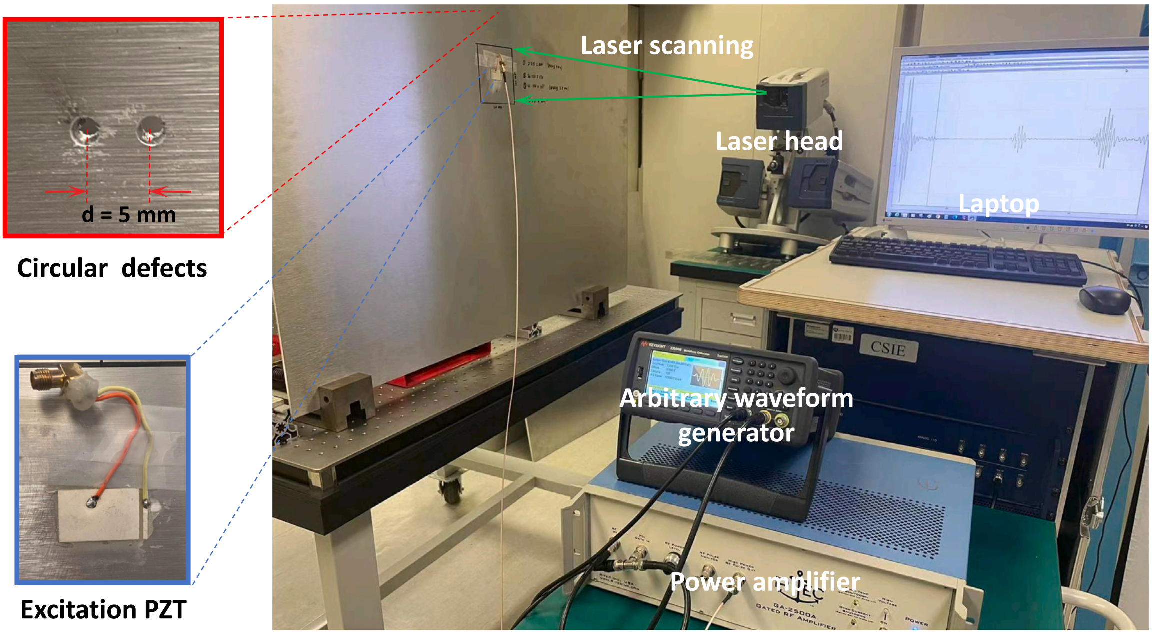

Fig. 13. The experimental setup involved the collection of ultrasonics lamb wave signals and focused on a specific region of interest within a tested aluminum plate.

experimental tolerances. These results indicate the super-resolution capability of the proposed method in the presence of experimental uncertainties such as measurement noise and boundary reflections.

To further examine the robustness of the proposed framework, a series of experiments were conducted by systematically varying two key *practical* parameters: the scan aperture and sensor spacing. These experiments were designed to mirror the numerical parametric studies and to assess the sensitivity of the reconstruction to changes in measurement configuration. The corresponding imaging results (Fig. 15) clearly demonstrate that the LWD-FISTA algorithm maintains reliable defect separability across a range of aperture sizes and spatial sampling densities.

Discussion: From a physical perspective, reducing the scan aperture constrains the effective angular coverage of the sensing array, leading to a broadened system PSF and a corresponding degradation in lateral resolution. Despite this fundamental limitation, the proposed LWD-FISTA algorithm remains capable of resolving the two closely spaced defects, underscoring its ability to partially overcome diffraction-induced blurring through physics-informed deconvolution.

Similarly, decreasing the sensor spacing increases the spatial sampling density of the Lamb wave field, allowing higher spatial frequency

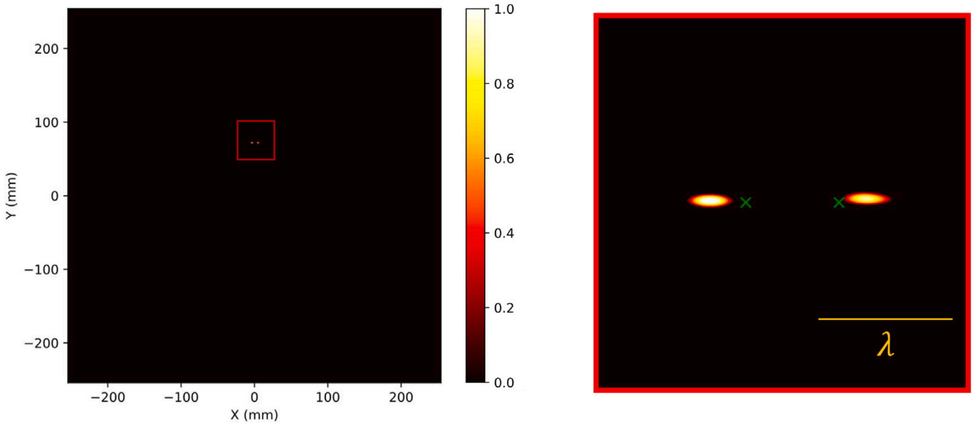

Fig. 14. The image is a LWD-FISTA result in experimental validation of subwavelength defect detection. Aperture size is 100 mm and sensor spacing is 5 mm.

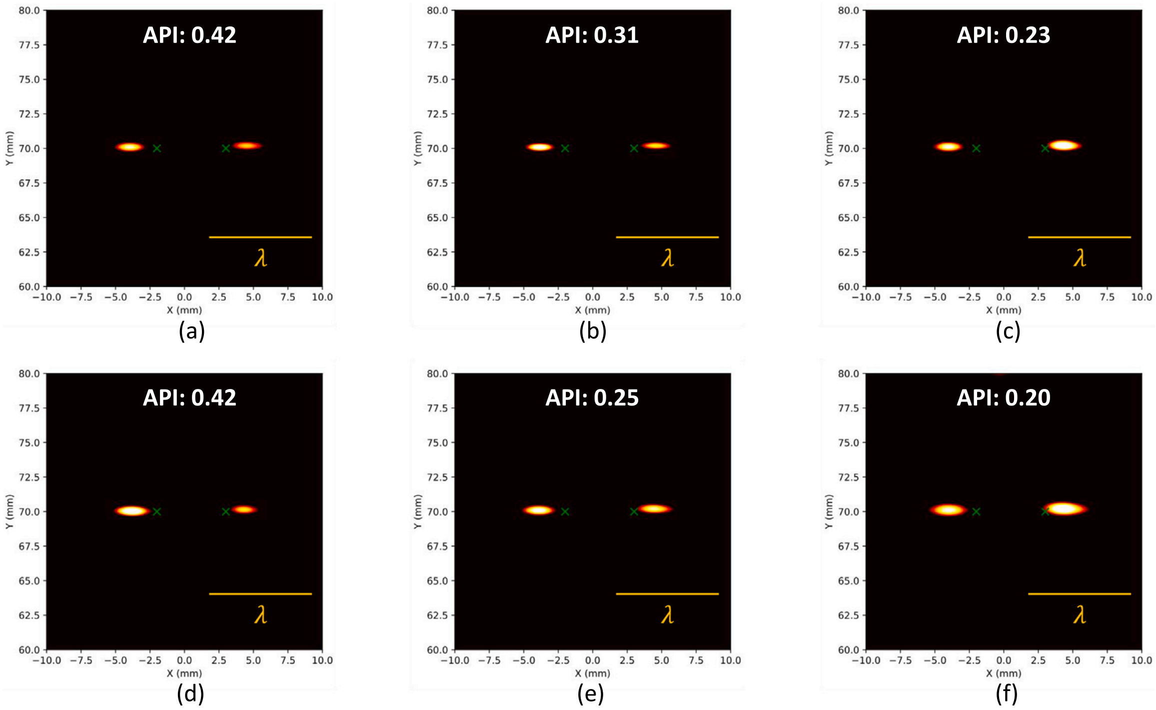

Fig. 15. The images in the upper row are scanned with a scan side length of 80 mm and (a) sensor spacing of 10 mm, (b) sensor spacing of 5 mm and (c) sensor spacing of 2.5 mm. The images in the bottom row are scanned with a side length of 100 mm, (d) sensor spacing of 10 mm, (e) sensor spacing of 5 mm and (f) sensor spacing of 2.5 mm.

components to be captured and resulting in sharper, more artifact-free reconstructions. This enhanced sampling fidelity leads to clearer defect boundaries and improved localization accuracy, experimentally confirming that adequate spatial sampling is essential for achieving high-quality super-resolution imaging.

4.1. Comparison with representative deep learning-based super-resolution methods

Recent deep learning-based super-resolution Lamb-wave imaging methods have shown promising performance, particularly for subwavelength defect reconstruction using multiscale learned priors and, more recently, Bayesian uncertainty-aware networks. However, their imaging mechanism differs fundamentally from that of the present study.

To better position the present work relative to representative learning-based approaches, Table 1 summarizes a methodological comparison between representative learning-based Lamb-wave super-resolution approaches and the proposed LWD-FISTA framework, in order to clarify the distinct role of the present physics-informed and training-free formulation. The comparison is informative in clarifying the practical role of the proposed method. In particular, unlike learning-based approaches, LWD-FISTA does not require offline training or labeled datasets, and can be directly deployed once the target-mode dispersion relation is specified. Under the present experimental configuration, the proposed method successfully resolves two closely spaced defects with a center-to-center spacing of 5 mm, which is below the diffraction-limited baseline of conventional TFM (approximately 7 mm for the A_0-dominated case at 200 kHz under the present aperture setting). These observations suggest that the proposed method should be viewed as a physics-based and training-free complement to deep learning-based super-resolution imaging, with particular advantages in physical interpretability, reduced data dependence, and direct deployability across measurement conditions.

Table 1
Comparison between representative deep learning-based Lamb-wave super-resolution methods and the proposed LWD-FISTA framework.

Method	Generalization	Train	Retraining burden	Physical interpretability	Uncert.	Deployment flexibility
Multiscale deep learning	Moderate	Strong	Strong	Limited	Limited	Moderate
Bayesian deep learning	Moderate	Strong	Strong	Limited	Strong	Moderate
Proposed LWD-FISTA	Strong	Limited	Limited	Strong	Limited	Strong

5. Conclusion and future work

Conventional ultrasonic array imaging methods, including the TFM, are inherently constrained by diffraction, which manifests through the finite mainlobe width and sidelobe structure of the system PSF and limits the reliable separation of closely-spaced defects. In Lamb-wave-based imaging, this challenge is further compounded by strong modal and frequency dispersion, which fundamentally distorts the PSF and invalidates conventional shift-invariant assumptions.

In this work, we present that super-resolution imaging in guided-wave NDT may be achieved through a physics-informed inversion of the imaging system response. By explicitly incorporating Lamb-wave dispersion into PSF modeling and embedding this dispersion-informed PSF into a deconvolution framework, the proposed approach effectively suppresses sidelobe interference and contracts the effective PSF mainlobe, thereby enabling reliable defect separation beyond the classical diffraction limit while preserving the intrinsic noise robustness of TFM.

The proposed framework was validated through both finite element simulations and laboratory experiments on aluminum plates. Systematic parametric studies reveal that the attainable super-resolution performance is jointly governed by physical and sampling constraints. Specifically, increasing the effective aperture enhances angular coverage and spatial bandwidth, leading to a narrower PSF; while sufficiently dense sensor spacing is essential to preserve wavefield fidelity and prevent spatial aliasing that degrades deconvolution accuracy. Furthermore, comparative studies with the TR-MUSIC algorithm show that the proposed method exhibits remarkable robustness under low-SNR conditions, maintaining reliable defect separability at SNR levels as low as 0 dB.

Collectively, these results indicate that the key to achieving super-resolution Lamb-wave imaging lies in physically consistent PSF modeling and inversion, with the deconvolution solver serving as an enabling computational tool. Thus, the proposed dispersion-informed framework may provide an effective alternative for practical NDT scenarios characterized by limited aperture, sparse measurements, and strong noise contamination.

Some challenges associated with applying the proposed method are also observed in this study. First, it was observed that while the proposed framework is highly effective for isolated subwavelength defects, its extension to spatially distributed damage patterns, such as corrosion and irregular material loss, introduces additional challenges related to PSF variability and model mismatch. Addressing these issues motivates several directions for future research. In particular, the proposed dispersion-informed deconvolution framework will be extended to more complex damage scenarios, including distributed corrosion, subwavelength defects with irregular geometries. Moreover, future work will extend the current single-mode formulation toward more challenging cases involving severe multimode aliasing, higher-frequency excitation, and structurally complex media such as anisotropic composite laminates, where multimode and anisotropy-aware forward models may be required.

CRediT authorship contribution statement

Tingjian Li: Writing – original draft, Validation, Software, Methodology, Investigation, Formal analysis. **Shanwu Li:** Writing – review & editing, Validation, Methodology, Investigation. **Shengbo Shan:** Writing – review & editing, Resources, Investigation. **Li Cheng:** Writing – review & editing, Supervision, Resources, Investigation. **Yongchao Yang:** Writing – review & editing, Validation, Supervision, Resources, Project administration, Methodology, Investigation, Funding acquisition, Conceptualization.

Declaration of competing interest

The authors declare that they have no known competing financial interests or personal relationships that could have appeared to influence the work reported in this paper.

Acknowledgment

The research was partially funded by the National Key Research and Development Program of China (Grant No. 2024YFC3808604), and the Key Program of the Natural Science Foundation of Zhejiang (Grant No. LZ25E080001).

Appendix. The deconvolution algorithm

This appendix briefly summarizes the numerical solvers employed to efficiently compute the dispersion-informed deconvolution problem presented in the main text. In particular, we outline the FFT-based non-negative least squares (FFT-NNLS) formulation and its accelerated solution using the Fast Iterative Shrinkage-Thresholding Algorithm (FISTA). These algorithms serve as numerical solvers for the proposed physics-informed inverse model, enabling computationally efficient reconstruction for large-scale Lamb-wave imaging problems, without altering the underlying physical formulation.

The resulting constrained optimization problem is given by

$$\min_{B_{\text{clean}}\geq 0}\frac{1}{2}\left\|\mathcal{F}^{-1}\left(\mathcal{F}\left(B_{clean}\right)\Theta\mathcal{F}\left(P_{dis}\right)\right)-B_{dirty}\right\|_F^2 \tag{A.1}$$

where $\|\cdot\|$ denotes the Frobenius norm.

Owing to the high dimensionality of practical imaging problems, first-order optimization methods are typically adopted to achieve computationally efficient solutions [45]. The optimization problem in Eq. (A.1) corresponds to a NNLS formulation [38]. To efficiently solve this large-scale inverse problem, we adopt the FISTA, an accelerated first-order method well suited for convex problems with composite objectives [46]. The smooth part of the objective function is given by

$$\begin{aligned}\frac{1}{2}\left\|\mathcal{F}^{-1}\left(\mathcal{F}\left(B_{clean}\right)\Theta\mathcal{F}\left(P_{dis}\right)\right)-B_{dirty}\right\|_F^2\\+\frac{\alpha}{2}\left\|D\cdot B_{clean}\right\|_F^2\end{aligned} \tag{A.2}$$

Efficient implementation of FISTA requires estimation of the Lipschitz constant L_1 of the gradient $\nabla f(\cdot)$. It is widely recognized that for $\psi(x) = \frac{1}{2}\|Ax-b\|_F^2$ is a smooth and unconstrained quadratic function [42], a Lipschitz constant is the maximum eigenvalue λ_{max} of the Hessian matrix $\nabla^2\psi = A^TA$ and it can therefore be estimated using the power method [43]. Regarding the power method, its convergence rate is determined by the ratio of the largest eigenvalue to the second eigenvalue. Further discussion on the convergence properties can be found in Golub and Van Loan [47]. Similarly, the Lipschitz constant in Eq. (A.2) can also be efficiently estimated.

The FISTA iterations are terminated when either the relative change between two consecutive iterates falls below a prescribed tolerance or the maximum iteration number is reached. Specifically, the convergence criterion is defined as

$$\frac{\|B_{clean}^{(k+1)} - B_{clean}^{(k)}\|_F}{\max(\|B_{clean}^{(k)}\|_F, \epsilon_0)} < \epsilon_{\text{tol}} \tag{A.3}$$

where ϵ_{tol} is the convergence tolerance, and ϵ_0 is a small positive constant introduced to avoid division by zero. In the present work, the iterative process is stopped when Eq. (A.3) is satisfied or when the iteration number reaches $K_{\max}$. In all reconstructions reported in this study, we set $\epsilon_{\text{tol}} = 1e^{-5}$ and $K_{\max} = 100$.

Data availability

Data will be made available on request.

References

[1] Giurgiutiu V, Bao J. Embedded-ultrasonics structural radar for in situ structural health monitoring of thin-wall structures. Struct Health Monit 2004;3(2):121–40.
[2] Holmes C, Drinkwater BW, Wilcox PD. Post-processing of the full matrix of ultrasonic transmit–receive array data for non-destructive evaluation. NDT E Int 2005;38(8):701–11.
[3] Su Z, Ye L, Lu Y. Guided lamb waves for identification of damage in composite structures: A review. J Sound Vib 2006;295(3–5):753–80.
[4] Giurgiutiu V. Structural health monitoring: with piezoelectric wafer active sensors. Elsevier; 2007.
[5] Yu L, Giurgiutiu V. In situ 2-D piezoelectric wafer active sensors arrays for guided wave damage detection. Ultrasonics 2008;48(2):117–34.
[6] Jeon JY, Kim D, Park G, Flynn E, Kang T, Han S. 2D-wavelet wavenumber filtering for structural damage detection using full steady-state wavefield laser scanning. NDT E Int 2020;116:102343.
[7] Flynn EB, Chong SY, Jarmer GJ, Lee J-R. Structural imaging through local wavenumber estimation of guided waves. Ndt E Int 2013;59:1–10.
[8] Flynn EB, Stull ND. Toward utilizing full-field laser-ultrasound for practical nondestructive inspection with acoustic wavenumber spectroscopy. In: 2018 IEEE international ultrasonics symposium. IUS, IEEE; 2018, p. 1–7.
[9] Wang CH, Rose JT, Chang F-K. A synthetic time-reversal imaging method for structural health monitoring. Smart Mater Struct 2004;13(2):415.
[10] Drinkwater BW, Wilcox PD. Ultrasonic arrays for non-destructive evaluation: A review. NDT E Int 2006;39(7):525–41.
[11] Yu L, Tian Z. Guided wave phased array beamforming and imaging in composite plates. Ultrasonics 2016;68:43–53.
[12] Tian Z, Howden S, Ma Z, Xiao W, Yu L. Pulsed laser-scanning laser Doppler vibrometer (PL-SLDV) phased arrays for damage detection in aluminum plates. Mech Syst Signal Process 2019;121:158–70.
[13] Song H, Yang Y. Accelerated noncontact guided wave array imaging via sparse array data reconstruction. Ultrasonics 2022;121:106672.
[14] Zhu W, Xiang Y, Zhang H, Zhang M, Fan G, Zhang H. Super-resolution ultrasonic Lamb wave imaging based on sign coherence factor and total focusing method. Mech Syst Signal Process 2023;190:110121.
[15] Gruber FK, Marengo EA, Devaney AJ. Time-reversal imaging with multiple signal classification considering multiple scattering between the targets. J Acoust Soc Am 2004;115(6):3042–7.
[16] Marengo EA, Gruber FK, Simonetti F. Time-reversal MUSIC imaging of extended targets. IEEE Trans Image Process 2007;16(8):1967–84.
[17] Labyed Y, Huang L. Ultrasound time-reversal MUSIC imaging with diffraction and attenuation compensation. IEEE Trans Ultrason Ferroelectr Freq Control 2012;59(10):2186–200.
[18] Prado VT, Higuti RT, Kitano C, Martínez-Graullera Ó, Adamowski JC. Lamb mode diversity imaging for non-destructive testing of plate-like structures. Ndt E Int 2013;59:86–95.
[19] Ducousso M, Reverdy F. Real-time imaging of microcracks on metallic surface using total focusing method and plane wave imaging with Rayleigh waves. NDT E Int 2020;116:102311.
[20] Camacho J, Atehortua D, Cruza J, Brizuela J, Ealo J. Ultrasonic crack evaluation by phase coherence processing and TFM and its application to online monitoring in fatigue tests. Ndt E Int 2018;93:164–74.
[21] Xu C, Deng M. Waveform correlation factor (WCF) weighted TFM imaging for lamb wave phased array. NDT E Int 2022;129:102647.
[22] Yu S, Fan C, Zhang M, Zhao Y. A Lamb wave time-reversal field reconstruction method for damage detection with automatic focusing determination. Ultrasonics 2023;133:107030.
[23] Li B, Tian X, Shi W, Zhao B, Tan J. MTR-MUSIC: A Time-reversal based Super-resolution ultrasonic imaging method for multilayer structure defects. NDT E Int 2025;103493.
[24] Fan C, Caleap M, Pan M, Drinkwater BW. A comparison between ultrasonic array beamforming and super resolution imaging algorithms for non-destructive evaluation. Ultrasonics 2014;54(7):1842–50.
[25] Bao Q, Yuan S, Guo F. A new synthesis aperture-MUSIC algorithm for damage diagnosis on complex aircraft structures. Mech Syst Signal Process 2020;136:106491.
[26] Song H, Yang Y. Super-resolution visualization of subwavelength defects via deep learning-enhanced ultrasonic beamforming: A proof-of-principle study. NDT E Int 2020;116:102344.
[27] Song H, Yang Y. Noncontact super-resolution guided wave array imaging of subwavelength defects using a multiscale deep learning approach. Struct Health Monit 2021;20(4):1904–23.
[28] Zhang W, Chai X, Zhu W, Zheng S, Fan G, Li Z, Zhang H, Zhang H. Super-resolution reconstruction of ultrasonic Lamb wave TFM image via deep learning. Meas Sci Technol 2023;34(5):055406.
[29] Cantero-Chinchilla S, Wilcox PD, Croxford AJ. A deep learning based methodology for artefact identification and suppression with application to ultrasonic images. NDT E Int 2022;126:102575.
[30] Lin L, Xiao J, Zhang D, Liao J, Ma Z. Fast and high-resolution ultrasonic sparse TFM imaging based on cyclesr. Mech Syst Signal Process 2025;236:113030.
[31] Wang X, Lin M, Li J, Tong J, Huang X, Liang L, Fan Z, Liu Y. Ultrasonic guided wave imaging with deep learning: Applications in corrosion mapping. Mech Syst Signal Process 2022;169:108761.
[32] Zhang F, Luo L, Li J, Peng J, Zhang Y, Gao X. Ultrasonic adaptive plane wave high-resolution imaging based on convolutional neural network. NDT E Int 2023;138:102891.
[33] Fu S, Li M, Zhou L, He Y, Liu X, Hao X, Li Y. Deformable mirror based optimal PSF engineering for 3D super-resolution imaging. Opt Lett 2022;47(12):3031–4.
[34] Bajgholi ME, Rousseau G, Ginzel E, Viens M, Mélançon V. Developing flaw sizing methodology in total focusing method (TFM) by EDM calibration blocks. EJ Nondestruct Test 2024;10.
[35] Dougherty R. Extensions of DAMAS and benefits and limitations of deconvolution in beamforming. In: 11th AIAA/cEAS aeroacoustics conference. 2005, p. 2961.
[36] Brooks TF, Humphreys WM. A deconvolution approach for the mapping of acoustic sources (DAMAS) determined from phased microphone arrays. J Sound Vib 2006;294(4–5):856–79.
[37] Chu Z, Yang Y. Comparison of deconvolution methods for the visualization of acoustic sources based on cross-spectral imaging function beamforming. Mech Syst Signal Process 2014;48(1–2):404–22.
[38] Ehrenfried K, Koop L. Comparison of iterative deconvolution algorithms for the mapping of acoustic sources. AIAA J 2007;45(7):1584–95.
[39] Tiana-Roig E, Jacobsen F. Deconvolution for the localization of sound sources using a circular microphone array. J Acoust Soc Am 2013;134(3):2078–89.
[40] Xiang J, Dong Y, Yang Y. FISTA-Net: Learning a fast iterative shrinkage thresholding network for inverse problems in imaging. IEEE Trans Med Imaging 2021;40(5):1329–39.
[41] Chu N, Zhao H, Yu L, Huang Q, Ning Y. Fast and high-resolution acoustic beamforming: A convolution accelerated deconvolution implementation. IEEE Trans Instrum Meas 2020;70:1–15.
[42] Lylloff O, Fernández-Grande E, Agerkvist F, Hald J, Tiana Roig E, Andersen MS. Improving the efficiency of deconvolution algorithms for sound source localization. J Acoust Soc Am 2015;138(1):172–80.
[43] Ding X, Liang H, Jakobsson A, Tu X, Huang Y. High-resolution source localization exploiting the sparsity of the beamforming map. Signal Process 2022;192:108377.
[44] Hansen PC. Discrete inverse problems: insight and algorithms. SIAM; 2010.
[45] Nocedal J, Wright SJ. Numerical optimization. Springer; 1999.
[46] Beck A, Teboulle M. Gradient-based algorithms with applications to signal recovery. Convex Optim Signal Process Commun 2009;42–88.
[47] Golub GH, Van Loan CF. Matrix computations. JHU Press; 2013.